JOURNAL OF
biomaterials
applications

Hard Tissues and Materials

Journal of Biomaterials Applications
2019, Vol. 33(9) 1178–1194

DOI: 10.1177/0885328219825568
journals.sagepub.com/home/jba
SAGE

Corrosion and bone healing of Mg-Y-Zn-Zr-Ca alloy implants: Comparative in vivo study in a non-immobilized rat femoral fracture model

Da-Tren Chou[1], Daeho Hong[1], Sinan Oksuz[1], Riccardo Schweizer[1], Abhijit Roy[1], Boeun Lee[1], Puneeth Shridhar[1], Vijay Gorantla[1] and Prashant N Kumta[1,2,3,4,5]

Abstract

Biodegradable magnesium (Mg) alloys exhibit improved mechanical properties compared to degradable polymers while degrading in vivo circumventing the complications of permanent metals, obviating the need for surgical removal. This study investigated the safety and efficacy of Mg-Y-Zn-Zr-Ca (WZ42) alloy compared to non-degradable Ti6Al4V over a 14-week follow-up implanted as pins to fix a full osteotomy in rat femurs and as wires wrapped around the outside of the femurs as a cerclage. We used a fully load bearing model allowing implants to intentionally experience realistic loads without immobilization. To assess systemic toxicity, blood cell count and serum biochemical tests were performed. Livers and kidneys were harvested to observe any accumulation of alloying elements. Hard and soft tissues adjacent to the fracture site were also histologically examined. Degradation behavior and bone morphology were determined using micro-computed tomography scans. Corrosion occurred gradually, with degradation seen after two weeks of implantation with points of high stress observed near the fracture site ultimately resulting in WZ42 alloy pin fracture. At 14 weeks however, normal bone healing was observed in femurs fixed with the WZ42 alloy confirmed by the presence of osteoid, osteoblast activity, and new bone formation. Blood testing exhibited no significant changes arising from the WZ42 alloy compared to the two control groups. No recognizable differences in the morphology and more importantly, no accumulation of Mg, Zn, and Ca in the kidney and liver of rats were observed. These load bearing model results collectively taken, thus demonstrate the feasibility for use of the Mg-Y-Zn-Zr-Ca alloy for long bone fracture fixation applications.

Keywords

Magnesium biomaterial, Mg-Y-Zn-Zr-Ca alloy, biocompatibility, in vivo degradation, bone fracture healing

Introduction

Magnesium (Mg)-based high strength alloys have received escalated interest in the medical devices community for a variety of degradable implants, predominantly in orthopedic and craniofacial applications. Numerous studies in animals,[1] as well as recently humans[2,3] have overall shown the good biocompatibility of Mg alloys when implanted within or surrounding bone. These results combined with the comparable mechanical properties of Mg with natural bone[4] and its ability to degrade have made Mg and its alloys an attractive choice. Mg has

[1]Department of Bioengineering, University of Pittsburgh, Pittsburgh, PA, USA
[2]Department of Mechanical Engineering and Materials Science, University of Pittsburgh, Pittsburgh, PA, USA
[3]Department of Chemical and Petroleum Engineering, University of Pittsburgh, Pittsburgh, PA, USA
[4]Center for Craniofacial Regeneration, University of Pittsburgh, Pittsburgh, PA, USA
[5]Center for Complex Engineered Multifunctional Materials, University of Pittsburgh, PA, USA

Corresponding author:
Prashant N Kumta, Department of Bioengineering, Swanson School of Engineering, University of Pittsburgh, 815C Benedum Hall, 3700 O'Hara Street, Pittsburgh, PA 15261, USA.
Email: pkumta@pitt.edu

also been reported to have a positive influence on bone growth,[5–7] with in vivo studies showing higher bone mass found around the Mg bone implants compared to controls of polymeric or titanium implants.[6,8]

Among the in vivo studies reported to the best of our knowledge involving implantation of various Mg alloys into bone, the vast majority were implanted as rods, pins, or screws into the femoral diaphysis, with a few in the femoral condyle and marrow cavity.[1] Zhang et al. discovered the crucial role of Mg in promoting calcitonin gene-related polypeptide-α(CGRP)-mediated osteogenic differentiation that indicated the likely therapeutic role for Mg alloys in fracture healing.[8] Wu et al. also observed that Mg extract could promote the formation of osteoblasts with inhibitory effect on the differentiation of osteoclasts.[9] This in turn facilitates fracture healing of bones. In recent years, where investigators around the globe implanted pure Mg or Mg alloy into the bone, there are limited instances where Mg implant was used to bear the load to provide fixation for fractured bone. Typically, in a non-load bearing model, a hole is predrilled into the bone and the implant is then either press-fitted or screwed into place. Also, sometimes a bone fracture is created. In a load bearing model however, a full fracture is created in the bone and holes are predrilled into two sides of the fractured ulna to place plate and screw for fracture stabilization. Recently, Jahn et al. used Mg-2Ag pins in a mice model to support the fractured femora and determined that the use of Mg-2Ag pins significantly promoted callus formation at the fracture site.[10] Similar results were also seen in rabbit load bearing model for ulna fracture.[11,12]

In the current study however, our main focus is to pursue and analyze a fully load bearing model, wherein the complete fracture of the rat femur was intentionally only fixed using the implant pins of the Mg alloy, Mg-Y-Zn-Zr-Ca (WZ42) without any external fixation, and the performance was compared to that of the pins machined from the commonly used medical grade titanium alloy, Ti6Al4V. The model by intentional design bears the dual characteristics of exposing the system to considerable stress in the absence of any external immobilization, since the animal is allowed to ambulate immediately following surgery as well as creating ideal conditions for inducing stress corrosion to the implanted Mg alloy pins.

Previously, our group has explored yttrium (Y), zirconium (Zr) and calcium (Ca) as alloying elements to Mg.[13,14] Y is known to strengthen the grain boundaries of Mg alloys and improves the corrosion resistance when alloyed with Mg above 3 wt.%.[15–17] Mg-Y alloys were also recently studied in both in vitro and in vivo bone models showing good cytocompatibility results.[18] Zr serves as a good grain-refining agent, providing grain boundary strengthening and corrosion resistance.[19–24] Furthermore, Zn is well known to mechanically strengthen Mg through solid solution hardening mechanism.[25] In addition, Mg-Y-Zn has been explored previously for stent applications due to its good corrosion rate.[26,27] Recently, in vitro studies have also helped to understand the corrosion behavior and mechanism of Mg-Y-Zn-Zr alloys.[28,29] Ca is a major mineralized component in bone, and also improves corrosion resistance and mechanical properties of pure Mg up to addition of 1 wt.%.[30–32] In the past, density functional theory work conducted by our group has also demonstrated that alloying of Mg with Ca and Y favors the development of a stable and chemically less reactive hydroxide layer to impart greater corrosion resistance.[14] We therefore chose to use to study Mg-Y-Zn-Zr-Ca alloy in an in vivo model due to its superior mechanical strength and improvised corrosion resistance.[13]

Moreover, the load bearing model selected has conceptual similarities mimicking orthopedic fixation devices such as Kirschner wires (K-wires) and Steinmann pins – thin rods that are drilled or tapped through the bone fracture fragments to maintain the anatomical congruity and biomechanical stability required for optimal bone healing. Currently used stainless steel and titanium K-wires are removed after the bone has healed, necessitating a secondary removal procedure the patient must endure. To allow for easy removal of the K-wire during this secondary procedure, the ends of the rods are usually left outside the skin, forming a "pin-tract" that typically may act as a conduit for causing infection.[33–35] Other complications arising from these fixation devices include nerve injury, pain, osteomyelitis, and migration.[33,36–38] These shortcomings of K-wires and other common orthopedic devices derived customarily from existing inert metals could therefore be avoided through the use of degradable Mg alloys.

In addition to utilizing this challenging load bearing model with intramedullary fracture fixation pins, WZ42 wires were also wrapped around the mid-diaphysis region of un-fractured femurs forming a cerclage cuff. Our secondary objective is thus to also compare the degradation and tissue response to the Mg alloy implanted in different regions – WZ42 intramedullary pins versus WZ42 over-the-cortical-bone cuffs. With these two implants, in this study, we systematically assessed in vivo corrosion, bone healing, and host response to provide an overall evaluation of the degradable WZ42 Mg alloy when utilized in orthopedic device applications.

Materials and methods

Preparation of Mg-Y-Zn-Zr-Ca implants

The procedure for melting and casting the WZ42 alloy (nominal composition of Mg-4.0%Y-2.0%Zn-1.0%Zr-

0.6%Ca in wt. %) was conducted as described by our group previously.[13] Briefly, alloying elements in pure form and contained in Mg master alloys (Institute of Metal Research, Chinese Academy of Sciences, Shenyang, China) were melted in an electrical resistance furnace (Wenesco Inc., Chicago, IL, USA) under the protection of $Ar + 1.5\%$ SF_6 cover gas (Butler Gas Product, Pittsburgh, USA) and cast into a cylindrical mild steel mold preheated to 500°C after stirring and holding for 30 min to achieve dispersion of Zr.[13,39] After casting, a solution treatment of 400°C was applied for 20 h, and the ingot was quenched to room temperature in water to increase the alloy's ductility and homogenize the secondary phases.[32] The ingot was extruded at a temperature of 450°C with an extrusion ratio of 30 to improve the corrosion resistance and mechanical properties.[40] The extruded WZ42 and control material Ti6Al4V (Goodfellow Corporation, Coraopolis, PA, USA) were then lathe machined into pins with dimensions of 15 mm length- $\times$ 1.66 mm diameter. Thin wires of 20 mm length and 0.68 mm diameter from the lath machine were obtained, as the alloy was ductile enough to draw without rupture or fracture. Schematics and photographs of the machined pins and wire cuffs are shown in Figure 1. The implants were sonicated in washes of acetone and isopropanol and dried before undergoing sterilization by gamma radiation (2×10^6 cGy, 23.5 Gy/min, cesium 137 source, Mark I 68, JL Shepherd and Associates, San Fernando, CA, USA).

Surgical model and study protocol

All the animal experiments were approved by the University of Pittsburgh's Institutional Animal Care and Use Committee. Before surgery, female Sprague-Dawley rats weighing 250–300 g were anesthetized by inhalation of isoflurane at a concentration of 2–5% for initiation of sedation and 0.25–4% for maintenance. Only the right hind limb of each rat was operated. Photographs of the surgical procedure are shown in Figure 2. First, the right hind limbs were shaved and disinfected, and an approximately 2 cm incision was made over the dorsolateral right femur, with location indicated in Figure 2(a). The skin and mid-diaphysis region of the right femurs were exposed through a lateral approach. A complete femoral osteotomy was created using a circular saw (Figure 2(b)). The WZ42 or Ti6Al4V fixation pins were inserted first into the intramedullary space of the distal portion of the fractured femur (Figure 2(c)), and then inserted into the intramedullary space of the proximal femur (Figure 2(d)), with the fracture approximated as seen in Figure 2(e). In the case of the wire cuffs, the right femur was not cut, and the wires were wrapped around the midsection of the diaphysis over the periosteum and pressed against the bone to avoid any translation along the shaft of the femur or migration (Figure 2(g)). After the samples were implanted, the fascia and the muscles were closed with 3.0 VICRYL (J315), and the skin was closed using non-absorbable monofilament 3.0 polyamide sutures (Figure 2(f)).

Post-operative pain and distress were observed daily for expressions of stress and behavioral abnormalities, changes in movement, food, and water intake. Furthermore, the right hind limbs were clinically observed on a daily basis for any signs of infection, wound dehiscence, presence of gas pockets (GPs), or abnormal posture/thigh anatomy.

Groups of five animals for both WZ42 and Ti6Al4V pins were used for each time point of 2, 8, and 14 weeks postoperative respectively, for blood values, tissue samples (liver, kidney, femurs with surrounding soft tissues), and micro-computed tomography (μCT) analysis, and groups of six animals were implanted with wire cuffs with a single time point of 14 weeks for toxicological assessment, as displayed in Table 1. The number of animals (n) used per group per time point were determined following the published literature on testing of Mg alloys and evaluating their corrosion, biocompatibility, local and systemic toxicities, and other factors similar to this study.[10,41] The end point of this study (i.e. 14 weeks) was estimated based on the complete fracture healing time reported in the literature.[8,10] Immediately following sacrifice, the liver, kidney, and experimental group femurs were collected and stored for further analysis as described in the following sections. Three rats receiving no surgery were also sacrificed to serve as the naïve control group.

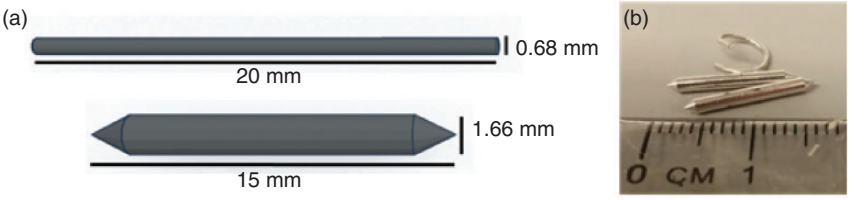

Figure 1. Schematic (a) and photograph (b) of sharpened pins (lower) inserted into the femoral intramedullary cavity and wire cuffs (upper) wrapped around the mid-diaphyseal region. In (a), the wire was machined straight and then coiled around the femur during surgery.

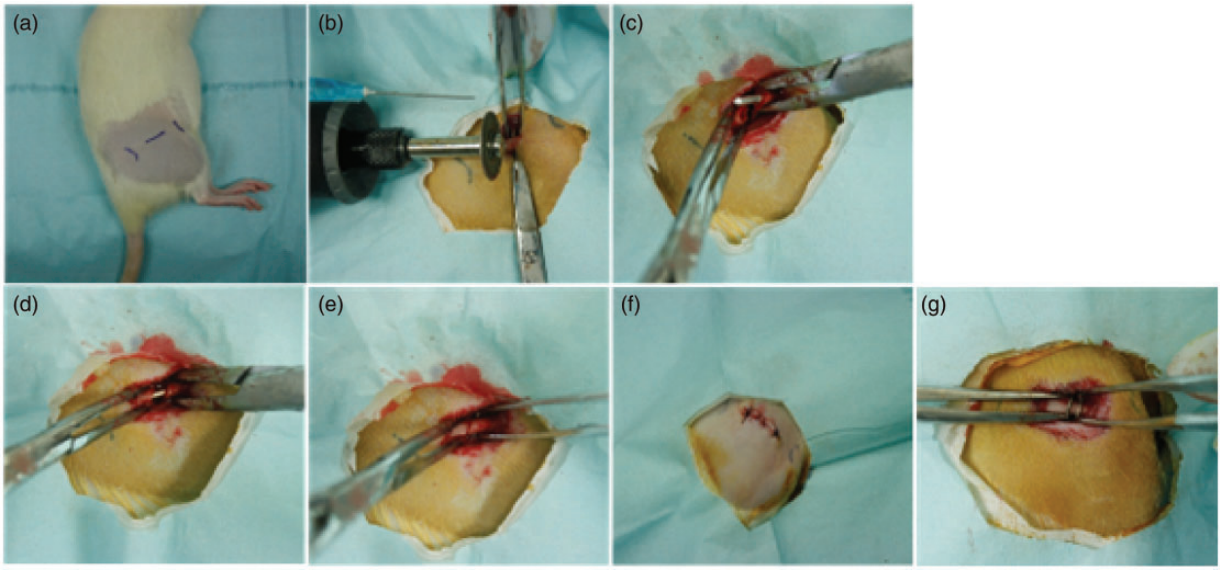

Figure 2. Surgical procedure used to implant metallic samples: (a) photograph of pins inserted into the femoral intramedullary cavity (bottom) and wire cuffs wrapped around the mid-diaphyseal region (top). Pin model – (a) markings indicating landmarks and the skin incision to expose the femur; (b) fracture being created in rat femur using circular saw; (c) pin inserted into marrow space of one side of fractured femur; (d) pin inserted into other side of femur create an intramedullary fixation; (e) fracture closed with pin maintaining alignment and fixation; (f) surgical site fully closed and sutured. Cuff model – (g) After skin incision and femur exposure, the bone was left intact without osteotomy, and a wire was wrapped around the midsection of the femur as a cerclage.

Table 1. Summary of number of rats in each group at time points used in study.

Time point:	Pre-operative	2 Weeks	8 Weeks	14 Weeks	14 Weeks
		Intramedullary pin			Cuff
Ti6Al4V		5	5	5	6
WZ42		5	5	5	6
Naïve	3				

X-ray imaging

Conventional X-ray imaging (Portable X-Ray SY-31–100, Soyee Products LLC, USA) was performed on rats only at one week post-operatively to examine the position of the implants and stability of the fracture. For that purpose, the animals were anesthetized with isoflurane. Conventional X-ray was not used to access the fracture healing of the rats with time.

Blood cell count and serum biochemical measurements

Blood samples were collected from animals before operation (baseline) under anesthesia by tail snip and terminally (2, 8, and 14 weeks post-implantation) by cardiac puncture. Whole blood cell counts were performed by Marshfield Labs (Cleveland, OH, USA) using a Sysmex XT2000i Automated Hematology Analyzer (Sysmex Corporation, Kobe, Japan) with provided reference ranges.[42] Serum samples were obtained by centrifuging collected blood at 2000 r/min for 10 min at 4°C. Serum biochemical tests were conducted by Marshfield Labs using an Olympus AU chemistry analyzer (Olympus Corporation, Tokyo, Japan) with reported reference ranges established by Marshfield Labs.

Micro-computed tomography imaging

Plastic embedded rat femurs were used for high-resolution μCT scanning (VivaCT40; Scanco Medical, Switzerland). WZ42 alloy samples were scanned with continuous rotation μCT at 10.5 μm voxel size before implantation and after retrieval along with surrounding tissue post-operatively at 2, 8, and 14 weeks. The reconstructed data sets were used to generate a 3D volume from which the remaining metal rod was distinguished from the surrounding degradation products and bone by using a histogram of grey values based on densities. A density threshold for the metal pins was

used to isolate the volume of remaining Mg alloy from the surrounding material and compared to the volume of the pins before implantation to estimate in vivo corrosion rate using the following equation adapted from the standard ASTM G31[43]

$$C = (K \times V)/(A \times T)$$

where C is the corrosion rate (mm year^{-1} or mmpy), the constant K is 8.76×10^4, V is the volume loss (cm^3), A is the initial sample area exposed (cm^2), and T is the time of exposure (h).

Histological preparation and analysis

Specimens of liver and kidney were fixed in 10% neutral buffered formalin, dehydrated, then infiltrated and embedded in paraffin. This was primarily done to rule out hepatotoxicity and renotoxicity, primarily due to rare earth elements such as Y. They were stained with hematoxylin and eosin (H&E) and investigated for cell infiltration, tissue morphology, and pathological changes due to the degradation and clearance of the WZ42 alloy in these critical visceral organs.

Femurs were fixed in 70% ethanol, dehydrated, and infiltrated and embedded in Osteo-Bed Plus methyl methacrylate-based embedding kit (Polysciences, Inc., Warrington, PA, USA). The plastic blocks were sectioned with a rotary microtome (Leica RM 2255, Leica Biosystems, Buffalo Grove, IL, USA) and stained using Goldner's Trichrome and alkaline phosphatase stains to observe bone morphology and osteoblast activity at the site of the fracture and surrounding the implants.[44] No quantitative analysis of the histological data was performed.

Tissue digestion and elemental analysis

Liver and kidney tissues were digested to allow for measurement of the elemental concentration using inductively coupled plasma with optical emission spectroscopy (ICP-OES). First, the tissues were dried at 70°C for 24 h, then homogenized and weighed. The samples were then digested by immersion in 20 ml nitric acid/g tissue for 6 h at 70°C, followed by the addition of 4 ml hydrogen peroxide/g tissue for 1 h and 4 ml sulfuric acid/g tissue for 1 h. Samples were then diluted 50× in ultra-pure deionized water (purified using Milli-Q Academic, Millipore, Billerica, MA, USA), filtered in 0.45 μm syringe filters, and analyzed for Mg and presence of various alloying element concentrations at 8 weeks and 14 weeks by ICP-OES (ICP-OES, iCAP duo 6500 Thermo Fisher, Waltham, MA, USA).

Statistical analysis

Statistical analysis was conducted using the SPSS Statistics 17.0 (SPSS Inc., Chicago, IL, USA). Differences between the groups were analyzed using one-way ANOVA with post-hoc testing using the Gabriel's pairwise test. $P < 0.05$ was accepted as a statistically significant difference between the means and is accordingly denoted in the figures. Error bars within the figures represent the standard deviation.

Results

Fixation of femoral fracture using Mg-Y-Zn-Zr-Ca alloy pin

The intramedullary pins were successfully inserted into the fractured femurs during surgery with the fractures being approximated as seen in the one-week postoperative X-ray images of Figure 3(a) to (c), despite the slight mismatches between the pin diameter and the diameter of the intramedullary cavity observed in 68% (13 of 19) of cases (Figure 3(b), red arrow) owing to manual surgical placement resulting in a small gap or misalignment in the two sides of the fractured femur. Also, it can be noted that the pins are larger in proportion to fractured bone site due to rat anatomical size restrictions. This may result in reduced osteogenic involvement of bone marrow-derived cells. All the wire cuffs, however, maintained their position wrapped around the femur as shown in Figure 3(d) and (e).

Small pockets of dead space, as seen in Figure 3(b), noted by the yellow arrow, were observed in the one-week X-rays of 73% (19 of 26) of the rats with implanted WZ42 alloy pins or cuffs, likely caused by the hydrogen gas evolved from the degrading Mg implants. Despite their presence in the X-ray images, no bulges in the skin in the hind limb of the rats were observed during the required frequent visual inspection of the rats during the study. The rats had regained mobility by postoperative day 7.

Systemic toxicity to Mg-Y-Zn-Zr-Ca implants

Total blood cell counts are listed in Table 2, which generally did not reveal any disturbance in the blood count values, with all parameters remaining within the reference ranges or near the pre-operation levels. Small differences from the reference ranges or naïve levels were observed for low platelet counts in the WZ42 cuff group, and WZ42 and Ti6Al4V pins at 14 weeks, while elevated postoperative white blood cell counts were seen at two weeks for both WZ42 and Ti6Al4V pins.

Similarly, serum biochemical parameters are shown in Table 3, with kidney function measured by creatinine

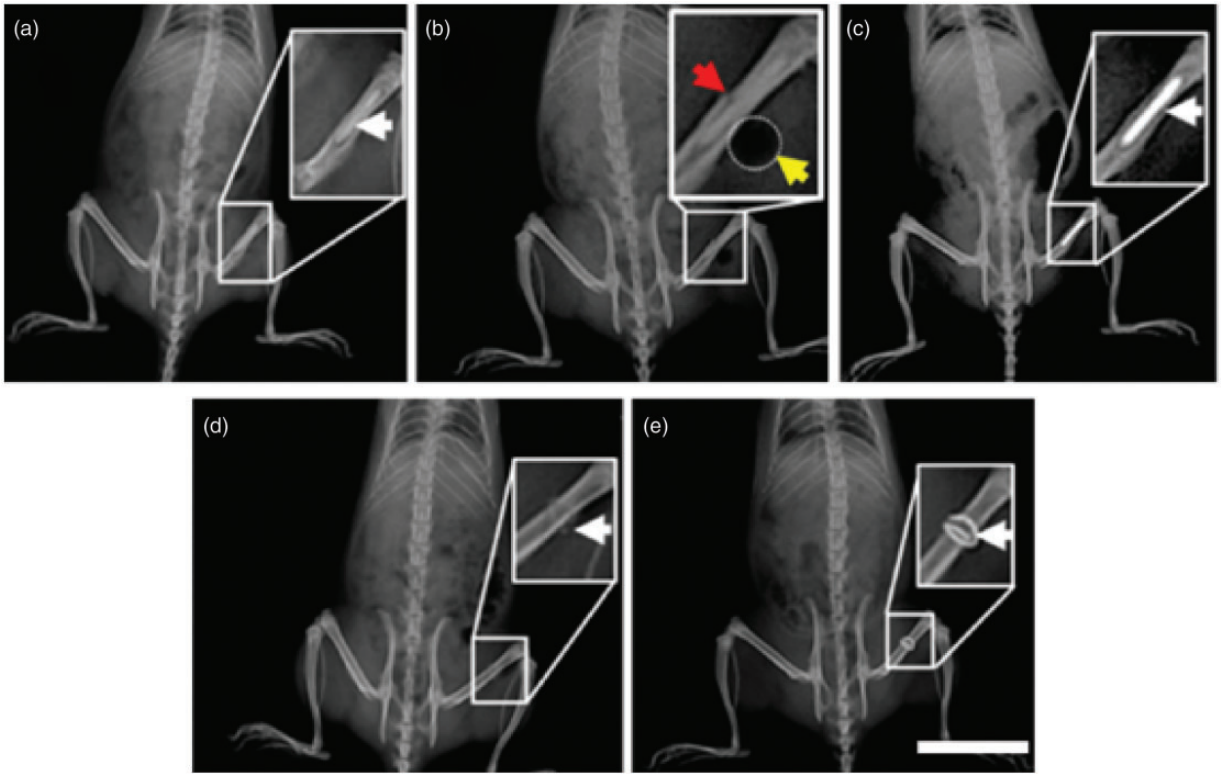

Figure 3. One-week postoperative X-ray images of implanted sharpened pins and cuffs (a) WZ42 pin in right femur of rats; (b) WZ42 pin in right femur of some rats showing fracture misalignment (red arrow) most likely due to thick nail and absence of pin locking mechanism and dead spaces (yellow arrow, circle) due to hydrogen gas formation; (c) Ti6Al4V pin (white arrow) in the right femur of rats (d) WZ42 wire cuff (white arrow) in right femur of rats showing maintenance of position and (e) Ti6Al4V wire cuff (white arrow) in the right femur of rats. Scale bar $\approx$ 5 cm.

Table 2. Average blood cell counts of naïve animals and animals implanted with WZ42 and Ti6Al4V alloy pins and cuffs at 2, 8, and 14 weeks after implantation.

Name	Implantation time	Red blood cell count	Hemoglobin	Platelet count	White blood cell count
Units		$10^6/\mu L$	g/dL	$10^3/\mu L$	$10^3/\mu L$
Ref. ranges		(7.00–9.00)	(13.7–16.8)	(680–1280)	(1.1–7.5)
Naïve		7.4 ± 0.3	14.1 ± 0.9	618.3 ± 200.6	6.8 ± 2.3
WZ42 pin	2 Weeks	8.0 ± 0.3	14.3 ± 0.6	839.0 ± 140.3	8.6 ± 1.5
Ti6Al4V pin	2 Weeks	7.8 ± 0.4	14.9 ± 0.7	656.0 ± 93.4	9.0 ± 1.2
WZ42 pin	8 Weeks	7.4 ± 0.5	13.8 ± 1.2	N/A	6.8
Ti6Al4V pin	8 Weeks	7.4 ± 0.3	14.2 ± 0.4	637.8 ± 168.6	5.9 ± 1.6
WZ42 pin	14 Weeks	7.7 ± 0.4	14.2 ± 0.5	595.8 ± 179.8	5.9 ± 2.1
Ti6Al4V pin	14 Weeks	7.5 ± 0.4	14.0 ± 0.7	563.0 ± 164.5	5.9 ± 2.7
WZ42 cuff	14 Weeks	7.1 ± 0.2	13.9 ± 0.4	461.0 ± 56.6	2.2 ± 1.0
Ti6Al4V cuff	14 Weeks	7.6 ± 0.4	13.8 ± 0.7	637.0 ± 96.5	5.8 ± 1.4

and urea levels, and liver function measured by the albumin, alkaline phosphatase, bilirubin, and glucose. All the parameters measured remained within the reference ranges or near the pre-operation levels, demonstrating little effect of the implanted alloy materials on the kidney and liver function as well as the metabolism.

Electrolyte parameters such as Ca, sodium, chloride, phosphorus, and Mg were measured from the serum samples, which are shown in Table 4. Importantly, Mg levels remained in the low end of the reference ranges, indicating no accumulation of the degrading Mg from the implants in the collected blood. All the other

Table 3. Average values of serum metabolic parameters of naïve animals and animals implanted with WZ42 and Ti6Al4V alloy pins and cuffs at 2, 8, and 14 weeks after implantation.

Name	Implantation time	Glucose	ALT(GPT)	ALP	Total Bilirubin	Total Protein	Albumin	Urea N	Creatinine	Globulin	A/G ratio
Units		mg/dL	U/L	U/L	mg/dL	g/dL	g/dL	mg/dL	mg/dL	g/Dl	
Ref. ranges		(70–308)	(59–166)	(232–632)	(0.0–0.1)	(5.8–7.1)	(3.2–3.7)	(13–19)	(0.3–0.5)	(2.6–3.5)	
Naïve		181.2 ± 19.8	55.8 ± 9.2	175.2 ± 20.3	0.17 ± 0.10	5.7 ± 0.1	3.3 ± 0.1	20.7 ± 1.9	0.37 ± 0.08	2.4 ± 0.1	1.4 ± 0.1
WZ42 pin	2 Weeks	155.8 ± 26.7	57.3 ± 7.9	148.3 ± 13.6	0.18 ± 0.05	6.3 ± 0.3	3.3 ± 0.2	20.3 ± 5.6	0.50 ± 0.00	3.0 ± 0.1	1.1 ± 0.1
Ti6Al4V pin	2 Weeks	322.0 ± 94.4	66.3 ± 20.3	151.2 ± 21.8	0.14 ± 0.05	6.2 ± 0.1	3.3 ± 0.1	17.6 ± 2.1	0.42 ± 0.04	2.9 ± 0.2	1.1 ± 0.1
WZ42 pin	8 Weeks	294.5 ± 205.0	80.4 ± 13.9	163.2 ± 30.4	0.24 ± 0.05	6.4 ± 0.3	3.5 ± 0.1	23.6 ± 2.1	0.52 ± 0.08	2.9 ± 0.3	1.2 ± 0.1
Ti6Al4V pin	8 Weeks	204.8 ± 75.9	54.5 ± 17.9	201.5 ± 40.2	0.18 ± 0.05	6.4 ± 0.3	3.7 ± 0.2	21.8 ± 2.9	0.53 ± 0.05	2.7 ± 0.1	1.3 ± 0.1
WZ42 pin	14 Weeks	177.8 ± 47.1	65.6 ± 8.7	183.8 ± 33.3	0.20 ± 0.00	6.4 ± 0.1	3.6 ± 0.1	22.2 ± 1.6	0.56 ± 0.05	2.7 ± 0.1	1.3 ± 0.1
Ti6Al4V pin	14 Weeks	229.5 ± 198.5	56.8 ± 15.8	187.0 ± 33.5	0.18 ± 0.04	6.3 ± 0.3	3.7 ± 0.2	21.8 ± 2.5	0.52 ± 0.04	2.6 ± 0.2	1.4 ± 0.1
WZ42 cuff	14 Weeks	123.6 ± 36.3	64.0 ± 7.7	155.2 ± 21.7	0.20 ± 0.00	6.3 ± 0.3	3.7 ± 0.2	24.8 ± 2.2	0.58 ± 0.04	2.6 ± 0.2	1.4 ± 0.1
Ti6Al4V cuff	14 Weeks	154.4 ± 53.6	50.2 ± 3.4	163.6 ± 30.3	0.18 ± 0.04	6.2 ± 0.3	3.6 ± 0.1	19.6 ± 1.9	0.52 ± 0.04	2.6 ± 0.2	1.4 ± 0.1

electrolytes similarly also remained consistent with the levels of the naïve rats and the prescribed allowable reference ranges.

ICP-OES results of the acid-digested liver and kidney (Figure 4) also demonstrated no accumulation of Mg (Figure 4(a)) exceeding the normal levels seen in the naïve control rats in the collected liver and kidney tissue in the WZ42 or Ti6Al4V groups. In fact, it was interesting to note lower concentration of Mg in the kidney tissues primarily in the WZ42 pin group when compared with naïve controls. Ca and Zn (Figure 4(b) and (c)) concentrations in the liver and kidney also did not deviate from the normal levels. Some differences were observed between the various groups; however, no significantly higher levels in the WZ42 groups of Mg, Ca, or Zn compared to naïve controls were observed. The concentrations of other alloying elements (Y and Zr) measured from the digested liver and kidney were also perceived to be too low to be differentiated from the control at 8 weeks and 14 weeks, with Y being present in $< 0.7\,\mu g/g$ dry mass in both the liver and kidney, and Zr present in $< 2.2\,\mu g$ dry mass in both the liver and kidney.

Histological examination of liver and kidneys

Conventional light microscopy images (Figure 5 for kidney and Figure 6 for liver) revealed that the cellular structure of the liver and kidney did not undergo any notable morphological changes or infiltration by inflammatory cells. No signs of any obvious abnormalities were also observed in any of the organ sections.

In vivo corrosion of Mg-Y-Zn-Zr-Ca alloy pins and morphology of surrounding bone

Representative cross-sectional μCT slices obtained from the femur-implant complex are shown in Figure 7.

After two weeks of implantation, all the implanted pins had broken as seen in Figure 7(a), despite all the pins appearing to be intact after one week as observed by X-ray (Figure 3). These pin failures occurred near the site of the femoral fracture, resulting in malunion. In addition, sites of pits of corrosion appeared at the junctions where the pins were clamped in collets during lathe machining seen in Figure 7(a). Both these two regions where the corrosion/failure occurred corresponded with the regions of likely higher stress, since the animals were allowed to ambulate immediately following surgery without any immobilization. One limitation of our study is that we did not perform quantitative analysis of the radiographical and histological information for fracture healing. Progressive degradation throughout the pins was observed at 8 and 14 weeks (Figure 7(b) and (c)). Regions of the

Table 4. Average values of electrolyte parameters of naïve animals and animals implanted with WZ42 and Ti6Al4V alloy pins and cuffs at 2, 8, and 14 weeks after implantation.

Name	Implantation time	Calcium	Sodium	Chloride	Phosphorus	Magnesium
Units		mg/dL	mmol/L	mmol/L	mg/dL	mg/dL
Ref. ranges		(9.5 – 13.9)	(146 – 151)	(98 – 104)	(5.6 – 16.8)	(3.8 – 5.5)
Naïve		9.8 ± 0.2	138.2 ± 1.9	100.5 ± 1.0	5.5 ± 0.2	2.0 ± 0.2
WZ42 pin	2 Weeks	11.2 ± 0.1	144.8 ± 1.7	101.0 ± 1.4	8.5 ± 0.9	2.9 ± 0.3
Ti6Al4V pin	2 Weeks	11.5 ± 0.5	143.8 ± 1.6	100.2 ± 2.2	9.7 ± 1.9	3.4 ± 0.4
WZ42 pin	8 Weeks	11.6 ± 0.5	144.4 ± 1.9	100.6 ± 2.8	9.7 ± 1.4	3.5 ± 0.5
Ti6Al4V pin	8 Weeks	11.8 ± 0.6	146.5 ± 1.0	100.0 ± 1.4	11.3 ± 0.8	3.9 ± 0.4
WZ42 pin	14 Weeks	11.4 ± 0.3	147.8 ± 1.9	100.2 ± 2.0	9.8 ± 0.7	3.6 ± 0.2
Ti6Al4V pin	14 Weeks	12.2 ± 1.1	145.2 ± 2.6	99.0 ± 2.0	9.6 ± 1.2	3.6 ± 0.6
WZ42 cuff	14 Weeks	11.3 ± 0.2	147.0 ± 0.7	101.4 ± 0.9	9.1 ± 1.4	3.2 ± 0.2
Ti6Al4V cuff	14 Weeks	11.6 ± 0.3	147.6 ± 1.1	99.6 ± 1.7	9.2 ± 0.7	3.3 ± 0.2

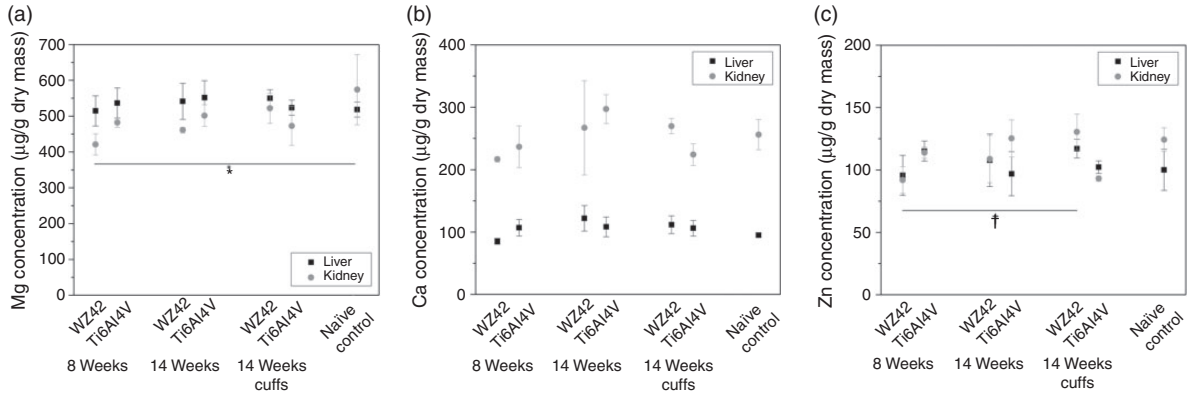

Figure 4. Average Mg (a), Ca (b), and Zn (c) concentration in digested liver and kidney samples of rats implanted with femoral pins and cuffs of WZ42 and Ti6Al4V for 8 and 14 weeks compared to naïve control rats. Significant difference * ($p < 0.05$) between Mg concentration in kidneys of rats implanted with WZ42 pins for eight weeks and naïve control rats and † ($p < 0.05$) between Zn concentrations in kidneys of rats implanted with WZ42 pins for eight weeks and cuffs. $n \leq 3$ per extract concentration per group per time point.

pin surrounded by the cortical bone appeared to degrade more slowly. µCT scans of the intact femurs with WZ42 wire cuffs wrapped around the midsection of the diaphysis (Figure 7(d)) revealed what appeared to be new bone (Nb) formation in the region surrounding the degrading cuffs indicated by arrows, despite the cuffs having completely degraded after 14 weeks when the scans were performed.

Following segmentation of the remaining WZ42 pins from the surrounding degraded product and bone, 3D reconstructions of the pins were created from which the volume was calculated. This remaining volume was used to calculate the corrosion rate at the end of the 2, 8, and 14 weeks as shown in Figure 8.

Degradation was found to occur more rapidly initially at two weeks, after which the corrosion rate was reduced and stabilized as seen by the lower corrosion rates calculated for 8 and 14 weeks. After the final time point of 14 weeks, approximately 43% of the original alloy pin volume remained.

Local tissue response to Mg-Y-Zn-Zr-Ca alloy pin

Femur explants were collected after 2, 8, and 14 weeks to assess the local tissue response to the WZ42 pins and cuffs and observe fracture healing. Sections of the bone from the femurs containing the pins were stained using the Goldner's Trichrome method and are shown in Figure 9.

After two weeks in rats implanted with the WZ42 alloy intramedullary pins, dead spaces were observed over the fracture site in the fibrous tissue (FT) ("soft callus") that had formed around the bone. This was likely due to the accumulation of hydrogen gas forming GPs from the degrading Mg alloy, as this was not observed in rats implanted with the Ti6Al4V pins. Osteoid (Od) had formed near the osteotomy region with FT surrounding the fracture site. After eight weeks, the empty pocket (dead space) over the fracture site was not perceived to be as prominent, potentially due to a slowing of the corrosion rate as measured by

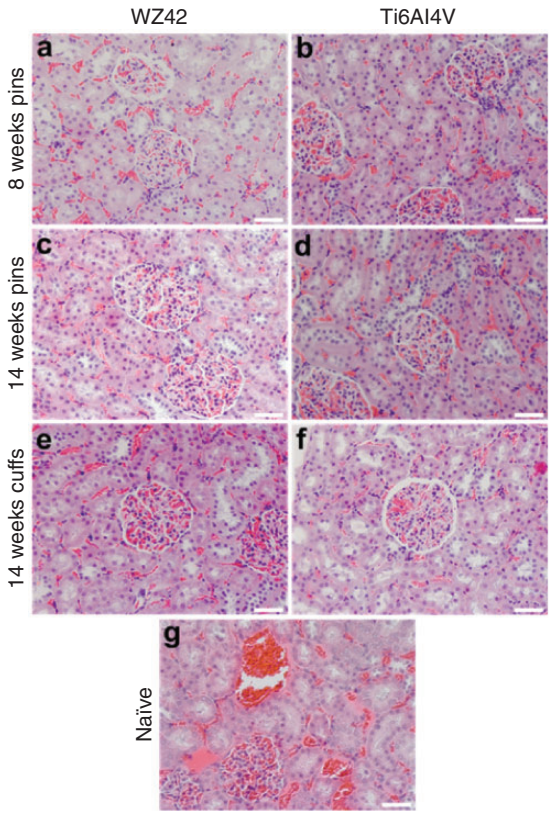

Figure 5. Representative photomicrographs of H&E stained kidneys of rats with femurs fixed by pins of WZ42 (a, c) and Ti6Al4V (b, d) after eight weeks (a, b) and 14 weeks (c, d). Stained images of kidneys from rats with implanted wire cuffs WZ42 (e) and Ti6Al4V (f) wrapped around bone for 14 weeks. Photomicrograph (g) of naïve rat. Scale bar = 50 μm.

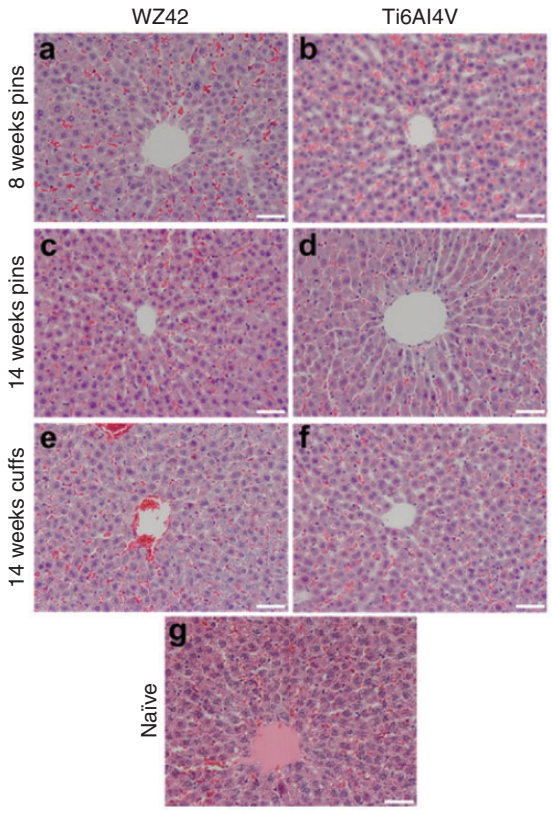

Figure 6. Representative photomicrographs of H&E stained livers of rats with femurs fixed by pins of WZ42 (a, c) and Ti6Al4V (b, d) after 8 weeks (a, b) and 14 weeks (c, d). Stained images of livers from rats implanted with wire cuffs of WZ42 (e) and Ti6Al4V (f) wrapped around bone for 14 weeks. Photomicrograph (g) from naïve rat. Scale bar = 50 μm.

μCT (Figure 8) along with accompanying dissipation of gas and ingrowth of FT. A greater presence of Od as well as Nb formation in the periosteal region was observed progressively at 8 and 14 weeks. At 14 weeks' post-implantation, in fact, the fracture was not completely healed when fixed with either WZ42 or Ti6Al4V pins with narrow gaps remaining between the fragments of cortical bone not yet filled by mature cortical bone.

Alkaline phosphatase staining was conducted to observe osteoblast activity and assess the process of Nb formation in the region surrounding the defect. Osteoblast activity was more abundant surrounding the fracture in the femurs containing WZ42 at 8 and 14 weeks (Figure 10(c) and (e)) compared to the femurs containing Ti6Al4V (Figure 10(d) and (f)). In fact, presence of osteoblasts appeared to peak at eight weeks for the WZ42 group.

Goldner's Trichrome stained sections of tissue near the site of wire cuff implantation (Figure 11) displayed Nb as seen in light blue-green as well as FT in the region surrounding the Mg alloy cuff implant (Figure 11(a)). In contrast, as expected, Nb formation was not seen around the inert Ti6Al4V cuff (Figure 11(b)).

Discussion

The work described herein illustrates the response of a new WZ42 Mg alloy when tested in a challenging fully load bearing in vivo model prone to considerable stress corrosion while at the same time demonstrating its biocompatibility despite the enhanced corrosion, without eliciting any toxicity. Moreover, the WZ42 alloy induced Nb formation and bone healing surrounding the fractured femur. The main animal model investigated in this work, a closed femoral fracture stabilized by an intramedullary pin, has been characterized by various groups studying the expression of genes for bone and cartilage matrix constituents[45] and growth factors,[46] the production of cytokines,[47] cell proliferation and apoptosis,[48,49] and to compare permanent metal pins for bone healing and mineralization.[50] Despite these instances of permanent metals such as stainless steel or Ni-Ti alloys being used to fix full

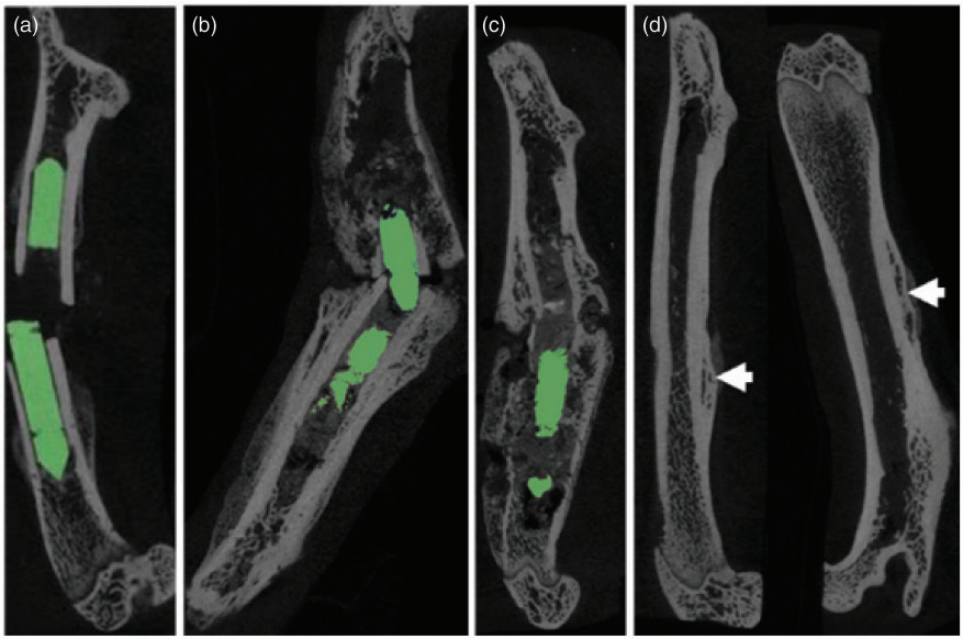

Figure 7. To determine the volume of the degrading WZ42 alloy, pins (highlighted in green) were distinguished from surrounding bone in micro-CT scans based on density thresholding with representative cross-sectional slices shown after implantation times of (a) two weeks, (b) eight weeks, and (c) 14 weeks. Cuffs were fully degraded after 14 weeks (d) but new bone formation was seen in the region the wires occupied (arrows).

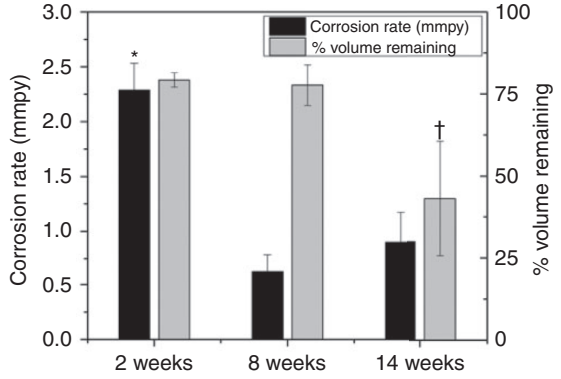

Figure 8. Corrosion rate and % volume remaining of WZ42 pins implanted into rat femurs for 2, 8, and 14 weeks. $n \geq 2$ for each group at each time point. * and † represent significant difference ($p < 0.05$) compared to measurements made at other time points.

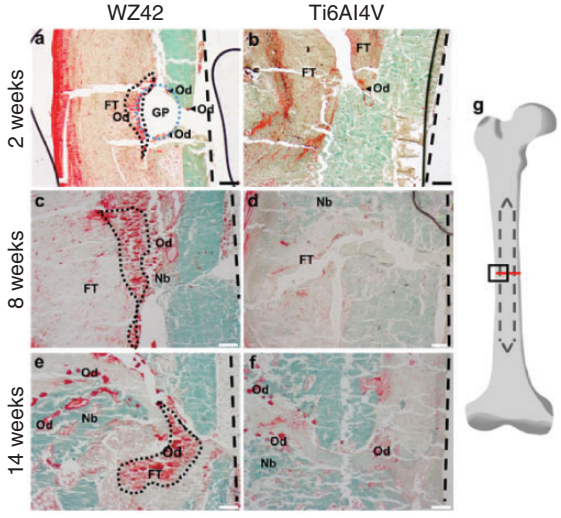

Figure 9. Photomicrographs of Goldner's Trichrome stained sections (40×) of soft and hard tissue at the femoral defect site fixed by pins of WZ42 magnesium alloy (a, c, e) and Ti6Al4V (b, d, f) after two weeks (a, b), eight weeks (c, d), and 14 weeks (e, f) of implantation; (g) representation of region of interest (black box) imaged along longitudinal plane at defect site. Cytoplasm, fibrin, muscle, and Ods are represented in red; collagen and bone are represented in green. The dashed line approximates the implant pin–bone interface, the black dotted line approximates osteoid regions, and the blue dotted line approximates the gas pocket. Scale bar = 200 μm.
GP: gas pocket; Od: osteoids; FT: fibrous tissue; Nb: new bone.

osteotomies in rats, it should be noted that such an aggressive model representing non-immobilization of the fracture site following insertion of the pins and exposing the device to the presence of large dynamic stresses due to the ambulation of the animals immediately following surgery has been tested only in limited instances. In fact, very few models such as the one described herein of fully load bearing type has been applied extensively to a fracture fixation device

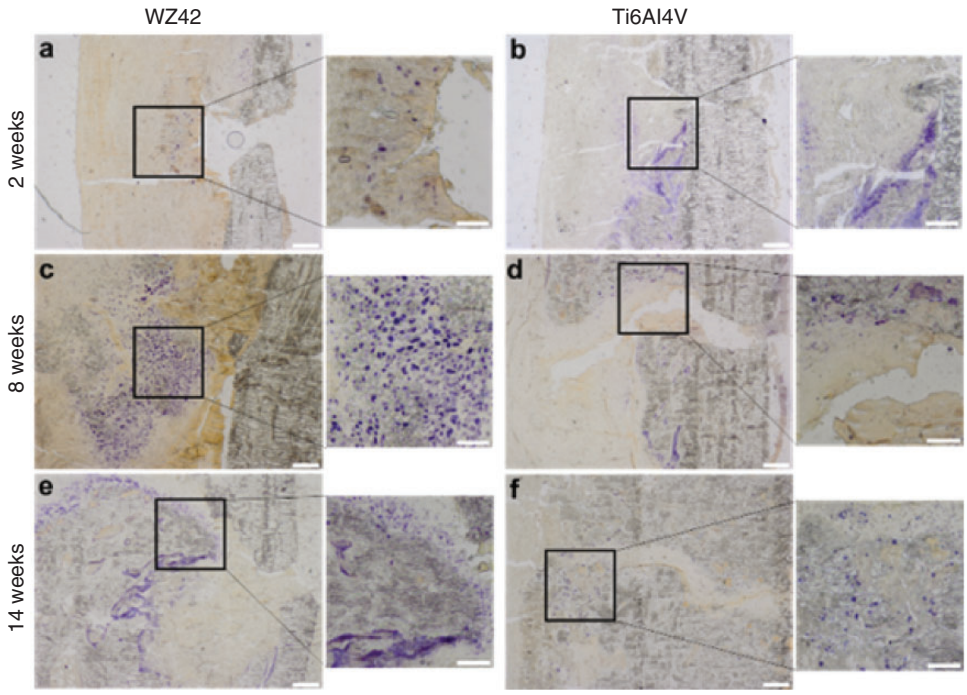

Figure 10. Photomicrographs of the localization of ALP (stained blue) at 40× and 100× (inset) of tissue at the femoral defect site fixed by pins of WZ42 magnesium alloy (a, c, e) and Ti6Al4V (b, d, f) after 2 weeks (a, b), 8 weeks (c, d), and 14 weeks (e, f) of implantation. Scale bar = 200 μm in 40× images, 100 μm in 100×. Pin located on right side all images.

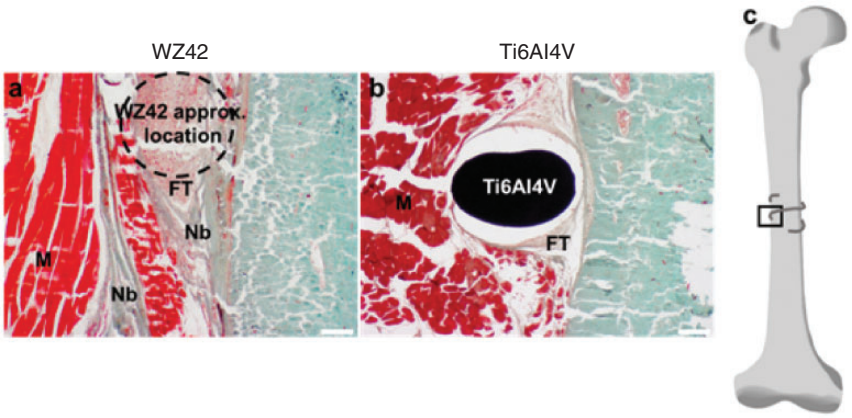

Figure 11. Photomicrographs of Goldner's Trichrome stained sections (40×) of soft and hard tissue at the implant–bone interface where wire cuffs of WZ42 magnesium alloy (a) and Ti6Al4V (b) were wrapped around bone for 14 weeks of implantation.
(c) Representation of region of interest (black box) imaged along longitudinal plane at defect site. Cytoplasm, fibrin, muscle, and osteoids are represented in red; collagen and bone are represented in green. The dashed line approximates the location of the WZ42 wire. Scale bar = 200 μm.
FT: fibrous tissue; Nb: new bone; M: muscle.

manufactured from Mg to date.[8,10,51] It was also the intent of this study to confirm the safety of WZ42 alloy in this challenging model and analyze the degradation behavior as a result of the high stress being placed on the Mg pins.

To assess the safety of the WZ42 implants, biochemical analysis of the blood and serum was conducted. The lower than expected platelet levels for the WZ42 and Ti6Al4V pin groups at 14 weeks and WZ42 wire cuff group also at 14 weeks was likely due to platelet clumping in samples, which was reported in many samples analyzed. The slightly elevated levels of white blood cells two weeks after surgeries for both WZ42 as well as Ti6Al4V represent a common post-surgical

inflammatory response known to occur during wound healing,[52] which returned to normal levels in the further follow-up evaluation; this was paralleled by evidence of no clinical signs of any surgical site infection. The consistent electrolyte levels as measured in blood and the stable Mg concentration measured in the digested kidney and liver signify that the degradation of WZ42 did not cause any disturbances in the balance of physiological electrolyte levels. Other studies have similarly found that blood biochemistry and liver and kidney function were not affected by Mg alloy degradation when implanted in bone, confirming the general safety of the degrading Mg alloys.[53–55] Along with the unaltered serum biochemical parameters suggesting that liver and kidney functions were not affected by the WZ42 alloy degradation, concentrations of Mg, Ca, and Zn (elements contained in the WZ42 alloy) in the liver and kidney also did not rise above the levels measured in naïve rats (Figure 4). Concentrations were also consistent with rats implanted with Ti6Al4V samples compared at the same time points.

To further demonstrate the systemic biocompatibility, H&E staining of liver and kidney samples did not reveal any signs of organ alteration or damage. No focal mineralization, acute inflammatory cell infiltration, or necrosis were observed in the kidney tissues. In the liver, no aggregates of inflammatory cells or features of hepatocellular necrosis, such as irregular patchy areas of coagulation necrosis were observed. These results suggest that the WZ42 alloy and its degradation products are systemically biocompatible. This is consistent with statements by Hartwig that an intake of high concentration of Mg ions would not cause any adverse reactions due to the high aptitude for the excretory system of the kidney and storage buffering capacity from bones to allow the body to maintain a balance of serum Mg.[56] Moreover, the biocompatibility and beneficial physiological roles of Mg, Ca and Zn in bone regeneration are well documented.[57–59] Y and other rare earth elements are commonly used as alloying elements to improve the corrosion resistance and biomechanical stability of the Mg[15–17]; however, the local and systemic toxicity as well as metabolic pathways of these elements are still unclear.[60,61] Recently, accumulation of traces of rare earth elements in the liver, kidney, and spleen of rabbits after 3.5 years of implantation has been reported.[62] It has also been demonstrated that the degradation of Y-containing alloy leads to the enrichment of Y concentration in the adjacent and newly formed bones.[63,64] However, the local Y-enrichment disappears with the complete degradation of the implant and bone remodeling with time. In this study, the lack of any detectable concentration of rare earth elements in the organs is possibly due to the very short duration of the study, and therefore, further studies will be required to demonstrate the complete absence of any systemic toxicity arising from this alloy.

Progressive degradation was observed in the intramedullary WZ42 pins as seen in the reducing cross-sectional area of the implants seen in Figure 7(a) to (c), and calculated corrosion rate and volume loss shown in Figure 8. Degradation appeared to occur preferentially at the fracture site, perpendicular to the fracture, where the stresses acting on the implanted pin are expected to be the highest. This synergy of mechanical loading combined with the corrosive environment of the surrounding fluids in the body has been shown to cause sudden fracture of implants via the stress corrosion cracking (SCC) mechanism.[65] This embrittlement phenomenon may occur even when the applied stress does not exceed the yield strength of the material, reducing the time to fracture and causing premature brittle failure. Mg, suffering from pitting corrosion, a source from which SCC can develop, has shown susceptibility to SCC in chloride solutions and simulated body fluids.[65,66] Other localized regions of corrosion, such as near the end of the pin in Figure 7(a), occurred due to pre-existing flaws likely imparted during the lathe machining that is indeed inevitable and unavoidable, which probably increased the susceptibility to SCC.[67]

Degradation at the site of fracture was also promoted by the higher exposure to the surrounding fluid electrolyte due to small gaps between the two sides of the femur, acting to produce fluid shear stress and remove local OH^- ions to reduce the protection that arises from the passivation layer.[68,69] During the early stages of healing after implantation when inflammatory responses were occurring, the characteristic hypoxic and acidic environment optimal for activities of polymorphonuclear leukocytes and tissue macrophages[70] would also result in higher corrosion rate due to the instability of the magnesium hydroxide in acidic conditions[71] and infiltration of these cells at the site of fracture causing phagocytosis of the metal debris.[72] After this initial inflammatory phase and more rapid corrosion rate occurring at two weeks, the corrosion appeared to slow down when measured at eight weeks as the surface of the Mg implant would become further passivated and the fracture site enclosed in FT, soft callus, and eventually newly formed bone, as observed in other studies of Mg implanted into bone.[73] During the bone repair progression, the pH rises ultimately becoming slightly alkaline to optimize alkaline phosphatase activity to perform its role in callus mineralization,[74] thereby becoming more conducive to the formation of the passivating

magnesium hydroxide layer on the surface of the degrading WZ42 pins.

The percentage volume remaining did not significantly change between two and eight weeks because the measurements were taken from different samples at each time point. For the implants used to calculate the eight-week measurements, the corrosion rate was lower, so that over time, the volume remaining ended up being not significantly different from the samples measured after two weeks which degraded at a much faster rate. The variation between the samples that caused the difference in degradation for two- versus eight-week samples may be due to variability when the pins failed, or pins not being fully surrounded by cortical bone due to malunion, thus being exposed to more surrounding fluid leading to enhanced corrosion. Surprisingly, at 14 weeks, the corrosion rate was observed to be relatively higher than that of eight weeks for the WZ42 pins. This may be due to the formation of smaller fragments of the pins which increases the overall effective surface area exposed to the surrounding fluids and therefore, increases the corrosion rate. The thin WZ42 cerclage wires wrapped around the outside of the femur, while being visually apparent in X-ray after one week (Figure 3(d)), were completely degraded after 14 weeks as seen in Figure 7(d) as a result of their smaller profile as well as being exposed to a much more corrosive environment having been placed on the surface of the femur instead of being surrounded by the cortical bone.

The effect of the degrading Mg alloy on the surrounding tissue was investigated via Goldner's Trichrome and ALP staining after 2, 8, and 14 weeks' post-implantation of the WZ42 and Ti6Al4V intramedullary pins and the extra-cortical cuffs. One major limitation of our study is that we compared pins versus cuffs that have a different design and dimension. The impact of this limitation could be, however, marginal considering that our goal was primarily to ascertain and compare qualitatively the individual biological responses of the pins and cuff. After two weeks in rats implanted with the WZ42 alloy (Figure 3(a), Figure 9 (a)), GPs were observed over the fracture site forming empty cavities in the surrounding in FT. This was likely due to accumulation of hydrogen gas from the degrading Mg alloy, as this is not observed in the Ti6Al4V pins. The accumulation of hydrogen gas from the Mg degradation reaction has been observed in numerous implant studies.[75,76] Despite potential concerns of the effects of these GPs on the healing processes,[76] no bone erosion due to these cavities was however, observed in the rabbits after one-year follow-up assessment of another Mg alloy also containing Mg, Y, and Zr[75] similar in composition to the WZ42 alloy used in the current work. After eight weeks (Figure 9(c)), the GP over the fracture site fixed with WZ42 was not as prominent, potentially due to slowing of the corrosion rate, absorption of gas, and accompanying ingrowth of FT. Clinical implantation of Mg alloy screws also revealed hydrogen gas formation soon after implantation, which disappeared through absorption into the surrounding tissue by approximately two to four weeks post-surgery.[3] Despite the appearance of hydrogen gas, the formation of calcification matrix was not inhibited to initiate the bone formation process, allowing for success in the long-term clinical study.[3]

The bone healing process of the fractured rat femurs was observed to consist of several phases as observed using the staining at various time points. After two weeks, the inflammatory phase of fracture healing that is inevitable appeared to have passed, with bone healing entering the reparative phase characterized by the development of callus tissue forming in and around the fracture site to be later replaced by bone.[77] The presence of Od was observed near the bone with FT to indicate the initial composition of the soft callus surrounding the fracture site. A greater presence of Od as well as Nb formation in the periosteal region was observed progressively after 8 and 14 weeks. After 14 weeks, the fracture was not yet completely healed with full woven bone when fixed with either WZ42 (Figure 9(e)) or Ti6Al4V (Figure 9(f)) pins; however, the presence of mineralized tissue indicated callus calcification as the mineralization process progressed.[78] The elevated Nb formation seen in the WZ42 group at 8 and 14 weeks was further confirmed by ALP staining (Figure 10), as ALP is necessary for mineralization of the callus providing phosphate ions for precipitation with Ca.[74] Osteoblast activity as indicated by ALP staining demonstrated promotion of Nb formation in the region surrounding the defect at the leading edge to heal the fracture. ALP activity peaked at eight weeks for the WZ42 group with higher activity compared to the Ti6Al4V group. Despite the fracture not having healed fully due to the instability of the intramedullary fixation devoid of any immobilization, the healing process did not appear to be encumbered or significantly compromised. It may be noted that, due to the pin size and the rat bone size constraints, the intramedullary pins were not fixed (locked) to support the fracture ends in our study which is typically seen in clinical treatment (nail with locking screws). We realized this might not avoid instability at the fracture sites and therefore, result in suboptimal healing. In fact, the prevalence of Nb formation as seen in the mineralized Nb and osteoblast activity in regions adjacent to the Mg alloy implants confirmed the results of numerous studies reporting enhanced Nb formation around Mg-based implants[6,11,12] related to the cellular activity of Mg such as osteoconductivity of the phosphate layer

forming on the surface of the Mg -based implants[55] and promotion of enhanced mineralization from the bone marrow stromal cells.[79] Additionally, the consistent observations of a normal healing response of a fibrous capsule enclosing the operation site with no abnormal presence of inflammatory cells at the implant site has been seen in other reports of Mg scaffolds showing good biocompatibility[80] and indicated the local biosafety of the Mg alloy. Without a defect created in the case of the wire cuff placed over the cortical bone, the phenomenon of enhanced Nb formation was confirmed in the region surrounding the Mg alloy cuff implant compared to the inert Ti6Al4V (Figure 11).

Overall, therefore, the positive biocompatibility and signs of healing with Nb formation observed in this study do suggest that the WZ42 alloy employed herein is indeed a suitable candidate for orthopedic applications, albeit with some caveats. Care must be taken, however, to ensure limiting the mechanical stresses placed on the implant and that a consistent finish on the alloy is obtained by careful machining so as to reduce the onset of rapid corrosion via pit formation and potential failure brought on by ensuing SCC. Immobilization of the fracture following implantation of the pins could certainly serve to alleviate the direct exposure of the implants to the extreme dynamic stresses leading to the accelerated corrosion likely limiting the complete bone formation and consequent fracture healing.

The model tested here in the absence of immobilization indeed provided an ideal environment contributing to creating a high dynamic stress on the implant site, thus loading the femur and completely transferring this load directly onto the Mg intramedullary pin, leading to a highly aggressive load and corrosion condition causing the pins to ultimately fail. The dynamic nature of the stresses combined with aggressive movement fostered by ambulation of the animals led to variation in the progression of the corrosion. As a result, variability in the non-union and healing could be seen (Figure 7(a) and (b)). This aggressive loading model, nevertheless, showed that despite having such an aggressive condition that could be perceived as an extreme event combined with accelerated corrosion, local and systemic biocompatibility of the alloy was still observed. Furthermore, although the corrosion rate was initially higher, hydrogen gas formation was fairly limited and not externally noticeable, while the surrounding tissue response, kidney and liver, and blood parameters all remained normal, thus alluding to the safety of these alloys. Hence, with temporary unloading and immobilization as is the standard of treatment for orthopedic injuries, the risk of failure of the WZ42 alloy would likely be diminished, still rendering the alloy as a promising orthopedic implant material, opening up possibilities for implementation in other medical device applications to be potentially explored. It is the opinion of the authors of this study that semi or non-load bearing environments placed on the orthopedic Mg implants would serve better to fully demonstrate their safety and efficacy in these settings before targeting more demanding, stressful applications such as the one reported here. Already, the pathway of lesser resistance has been observed by the reported success of Syntellix screws used for relatively low-risk hallux-valgus and scaphoid fracture procedures.[2,81] The work illustrated here and the model implemented without any harness albeit may not be ideal for fracture healing and bone formation but nevertheless, provides a compelling and definitive evidence attesting to the safety and non-toxicity of Mg and the alloying elements used to process the alloy to the extent of the size and dimensions used compared to the anatomical site and location of the defects in the rats employed in the current study.

More detailed studies in larger animals may be necessary, however, to further validate the safety and non-toxicity observed in the present study. Furthermore, it is necessary and critical to understand the mechanistic signaling pathways that would throw light on the enhancement of osteogenic bone response to Mg and its alloys in a load bearing environment. Another major drawback of the potential use of Mg alloys in general, is release of hydrogen GPs that can play a crucial role in the eventual use of implants in load bearing situation. We plan to overcome this limitation for translational applications of our alloys by focusing on the modification of surface characteristics of the alloys through chemical or physical modifications (e.g. anodization, surface coating) or use of combined engineered strategies.

Conclusions

WZ42 (Mg-Y-Zn-Zr-Ca) alloy pins were implanted into the intramedullary cavity of fractured rat femurs and as wires wrapped around the midsection of unaltered femurs, comparing the Mg alloy to Ti6Al4V. We found that the degradation of the intramedullary pins led to failure due to perceived stress-related corrosion initiated at the osteotomy site of high mechanical loading and surrounding vasculature aiding corrosion. However, the WZ42 alloy was still found to be biocompatible with no recognizable accumulation of Mg or alloying elements in the blood, liver, or kidney, and no adverse effects on blood count, or metabolic, kidney, and liver function. Histology of the local area at the implant site showed normal fracture healing and Nb formation. These positive results despite the challenging nature of the model indicated the promise of this particular alloy, WZ42, for orthopedic fixation

applications. Future studies may be directed to further optimize the alloy processing and composition techniques used with the primary goals of improving the corrosion and mechanical properties to avoid device failure. Additional animal studies in large animals to simulate the actual orthopedic device use with low or semi-load bearing environments, along with fracture stabilization (with screws and plates, especially biodegradable ones) will further validate the WZ42 alloy's safety and efficacy. Research in these directions will likely help advance the findings of the current research described in this paper with the aim of more widespread adoption of Mg alloys to improve the quality of treatment provided by orthopedic and craniofacial medical implants.

Acknowledgements

The authors gratefully thank the assistance from Dr. Yongjun Chen and Dr. Zhigang Xu of the North Carolina Agriculture and Technical University (NCA&T) for alloy extrusion.

Authors' Note

Data samples for this article can be provided upon request.
Sinan Oksuz was previously affiliated with Department of Plastic Surgery, University of Pittsburgh Medical Center, Pittsburgh, PA, USA and is now with the Department of Plastic Reconstructive and Aesthetic Surgery, Gulhane Medical School, University of Health Sciences, Ankara, Turkey.
Riccardo Schweizer was previously affiliated with Department of Plastic Surgery, University of Pittsburgh Medical Center, Pittsburgh, PA, USA and is now with Department of Plastic Surgery and Hand Surgery, University Hospital Zurich, Zurich, Switzerland.
Vijay Gorantla is now affiliated with Vascularized Composite Allotransplantation Program, Wake Forest Institute for Regenerative Medicine, Winston-Salem, NC, USA.

Declaration of Conflicting Interests

The author(s) declared no potential conflicts of interest with respect to the research, authorship, and/or publication of this article.

Funding

The author(s) disclosed receipt of the following financial support for the research, authorship, and/or publication of this article: The authors gratefully acknowledge the financial support of the U.S. National Science Foundation, Engineering Research Center – Revolutionizing Metallic Biomaterials, Grant #EEC-0812348 and the Commonwealth of PA Grant SAP#4100068505. PNK would like to acknowledge the Edward R. Weidlein Chair Professorship funds. The Center for Complex Engineered Materials for Multifunctional Materials (CCEMM), Swanson School of Engineering at the University of Pittsburgh is also acknowledged for providing the equipment and infrastructure needed to execute the work described.

ORCID iD

Prashant N Kumta http://orcid.org/0000-0003-1227-1249

References

1. Zheng YF, Gu XN and Witte F. Biodegradable metals. *Mater Sci Eng: R: Rep* 2014; 77: 1–34.
2. Windhagen H, Radtke K, Weizbauer A, et al. Biodegradable magnesium-based screw clinically equivalent to titanium screw in hallux valgus surgery: short term results of the first prospective, randomized, controlled clinical pilot study. *Biomed Eng Online* 2013; 12: 62.
3. Lee J-W, Han H-S, Han K-J, et al. Long-term clinical study and multiscale analysis of in vivo biodegradation mechanism of Mg alloy. *Proc Natl Acad Sci USA* 2016; 113: 716–721.
4. Staiger MP, Pietak AM, Huadmai J, et al. Magnesium and its alloys as orthopedic biomaterials: a review. *Biomaterials* 2006; 27: 1728–1734.
5. Groves EWH. An experimental study of the operative treatment of fractures. *Br J Surg* 1913; 1: 438–501.
6. Witte F, Kaese V, Haferkamp H, et al. In vivo corrosion of four magnesium alloys and the associated bone response. *Biomaterials* 2005; 26: 3557–3563.
7. Zreiqat H, Howlett CR, Zannettino A, et al. Mechanisms of magnesium-stimulated adhesion of osteoblastic cells to commonly used orthopaedic implants. *J Biomed Mater Res* 2002; 62: 175–184.
8. Zhang YF, Xu JK, Ruan YC, et al. Implant-derived magnesium induces local neuronal production of CGRP to improve bone-fracture healing in rats. *Nat Med* 2016; 22: 1160–1169.
9. Wu LL, Feyerabend F, Schilling AF, et al. Effects of extracellular magnesium extract on the proliferation and differentiation of human osteoblasts and osteoclasts in coculture. *Acta Biomater* 2015; 27: 294–304.
10. Jahn K, Saito H, Taipaleenmaki H, et al. Intramedullary Mg2Ag nails augment callus formation during fracture healing in mice. *Acta Biomater* 2016; 36: 350–360.
11. Chaya A, Yoshizawa S, Verdelis K, et al. In vivo study of magnesium plate and screw degradation and bone fracture healing. *Acta Biomater* 2015; 18: 262–269.
12. Chaya A, Yoshizawa S, Verdelis K, et al. Fracture healing using degradable magnesium fixation plates and screws. *J Oral Maxillofac Surg* 2015; 73: 295–305.
13. Chou DT, Hong D, Saha P, et al. In vitro and in vivo corrosion, cytocompatibility and mechanical properties of biodegradable Mg-Y-Ca-Zr alloys as implant materials. *Acta Biomater* 2013; 9: 8518–8533.
14. Velikokhatnyi OI and Kumta PN. First-principles studies on alloying and simplified thermodynamic aqueous chemical stability of calcium-, zinc-, aluminum-, yttrium- and iron-doped magnesium alloys. *Acta Biomater* 2010; 6: 1698–1704.
15. Wu AR and Xia CQ. Study of the microstructure and mechanical properties of Mg-rare earth alloys. *Mater Des* 2007; 28: 1963–1967.

16. Gao JC, Wu S, Qiao LY, et al. Corrosion behavior of Mg and Mg-Zn alloys in simulated body fluid. *Trans Nonferrous Met Soc China* 2008; 18: 588–592.
17. Liu M, Schmutz P, Uggowitzer PJ, et al. The influence of yttrium (Y) on the corrosion of Mg-Y binary alloys. *Corrosion Sci* 2010; 52: 3687–3701.
18. Bobe K, Willbold E, Morgenthal I, et al. In vitro and in vivo evaluation of biodegradable, open-porous scaffolds made of sintered magnesium W4 short fibres. *Acta Biomater* 2013; 9: 8611–8623.
19. Saha P and Viswanathan S. An analysis of the grain refinement of magnesium by zirconium. In: Sillekens WH, Agnew SR, Neelameggham NR, et al. (eds) *Magnesium technology 2011*. Cham: Springer International Publishing, 2011, pp.175–180.
20. Saha P and Viswanathan S. Engineering an efficient zirconium-based grain refiner for magnesium alloys. *Inter Metalcast* 2010; 4: 70–71.
21. Saha P, Lolies K, Viswanathan S, et al. A systematic study of the grain refinement of magnesium by zirconium. *Magnesium Technology* 2010; 425–430.
22. Saha P and Viswanathan S. Grain refinement of magnesium by zirconium: characterization and analysis. *American Foundry Society Proceedings* 2011; 119: 469–480.
23. Witte F, Hort N, Vogt C, et al. Degradable biomaterials based on magnesium corrosion. *Curr Opin Solid State Mat Sci* 2008; 12: 63–72.
24. Song G and St John D. The effect of zirconium grain refinement on the corrosion behaviour of magnesium-rare earth alloy MEZ. *J Light Metals* 2002; 2: 1–16.
25. Zhang SX, Zhang XN, Zhao CL, et al. Research on an Mg-Zn alloy as a degradable biomaterial. *Acta Biomater* 2010; 6: 626–640.
26. Hanzi AC, Gerber I, Schinhammer M, et al. On the in vitro and in vivo degradation performance and biological response of new biodegradable Mg-Y-Zn alloys. *Acta Biomater* 2010; 6: 1824–1833.
27. Hanzi AC, Sologubenko AS and Uggowitzer PJ. Design strategy for new biodegradable Mg-Y-Zn alloys for medical applications. *IJMR* 2009; 100: 1127–1136.
28. Bao L, Zhang ZQ, Le QC, et al. Corrosion behavior and mechanism of Mg-Y-Zn-Zr alloys with various Y/Zn mole ratios. *J Alloy Compd* 2017; 712: 15–23.
29. Fan J, Qiu X, Niu XD, et al. Microstructure, mechanical properties, in vitro degradation and cytotoxicity evaluations of Mg-1.5Y-1.2Zn-0.44Zr alloys for biodegradable metallic implants. *Mater Sci Eng C-Mater Biol Appl* 2013; 33: 2345–2352.
30. Ilich JZ and Kerstetter JE. Nutrition in bone health revisited: a story beyond calcium. *J Am Coll Nutr* 2000; 19: 715–737.
31. Drynda A, Hassel T, Hoehn R, et al. Development and biocompatibility of a novel corrodible fluoride-coated magnesium-calcium alloy with improved degradation kinetics and adequate mechanical properties for cardiovascular applications. *J Biomed Mater Res Part A* 2010; 93A: 763–775.
32. Li ZJ, Gu XN, Lou SQ, et al. The development of binary Mg-Ca alloys for use as biodegradable materials within bone. *Biomaterials* 2008; 29: 1329–1344.
33. Botte MJ, Davis JL, Rose BA, et al. Complications of smooth pin fixation of fractures and dislocations in the hand and wrist. *Clin Orthopaed Relat Res* 1992; 276: 194–201.
34. Hargreaves DG, Drew SJ and Eckersley R. Kirschner wire pin tract infection rates: a randomized controlled trial between percutaneous and buried wires. *J Hand Surg* (*Edinburgh, Scotland*) 2004; 29: 374–376.
35. Rafique A, Ghani S, Sadiq M, et al. Kirschner wire pin tract infection rates between percutaneous and buried wires in treating metacarpal and phalangeal fractures. *J Coll Phys Surg Pak* 2006; 16: 518–520.
36. Hochwald NL, Levine R and Tornetta P 3rd. The risks of Kirschner wire placement in the distal radius: a comparison of techniques. *J Hand Surg Am* 1997; 22: 580–584.
37. Sharma H, Taylor GR and Clarke NMP. A review of K-wire related complications in the emergency management of paediatric upper extremity trauma. *Ann R Coll Surg Engl* 2007; 89: 252–258.
38. Hsu LP, Schwartz EG, Kalainov DM, et al. Complications of K-wire fixation in procedures involving the hand and wrist. *J Hand Surg Am* 2011; 36: 610–616.
39. Qian M, StJohn DH and Frost MT. Zirconium alloying and grain refinement of magnesium alloys. In *Magnesium Technology 2003 as held at the 2003 TMS Annual Meeting 2003* (pp. 209–214).
40. Chou D-T. *Fundamental study of the development and evaluation of biodegradable Mg-Y-Ca-Zr based alloys as novel implant materials*. PhD Thesis, University of Pittsburgh, Pittsburgh, PA, 2016.
41. Gu XN, Xie XH, Li N, et al. In vitro and in vivo studies on a Mg-Sr binary alloy system developed as a new kind of biodegradable metal. *Acta Biomater* 2012; 8: 2360–2374.
42. Weiss DJ and Wardrop KJ. *Schalm's veterinary hematology*. Aimes, Iowa: Wiley, 2011.
43. Material ASfTa. *ASTM G31-72 standard practice for laboratory immersion corrosion testing of metals. Annual book of ASTM standards*. Philadelphia, PA: ASTM, 2004.
44. An YH and Gruber HE. Introduction to experimental bone and cartilage histology. In: YH An and KL Martin (eds) *Handbook of histology methods for bone and cartilage*. Totowa, NJ: Humana Press, 2003, pp.3–31.
45. Yamazaki M, Majeska RJ, Yoshioka H, et al. Spatial and temporal expression of fibril-forming minor collagen genes (types V and XI) during fracture healing. *J Orthop Res* 1997; 15: 757–764.
46. Bostrom MPG, Lane JM, Berberian WS, et al. Immunolocalization and expression of bone morphogenetic proteins 2 and 4 in fracture healing. *J Orthop Res* 1995; 13: 357–367.
47. Einhorn TA, Majeska RJ, Rush EB, et al. The expression of cytokine activity by fracture callus. *J Bone Miner Res* 1995; 10: 1272–1281.
48. Iwaki A, Jingushi S, Oda Y, et al. Localization and quantification of proliferating cells during rat fracture repair: detection of proliferating cell nuclear antigen by immunohistochemistry. *J Bone Miner Res* 1997; 12: 96–102.

49. Hausman MR, Schaffler MB and Majeska RJ. Prevention of fracture healing in rats by an inhibitor of angiogenesis. *Bone* 2001; 29: 560–564.
50. Ryhänen J, Kallioinen M, Serlo W, et al. Bone healing and mineralization of femoral osteotomy fixed with intramedullary NiTi rod. *SMST-2000: proceedings of the international conference on shape memory and superelastic technologies*. Materials Park, OH, USA: ASM International, 2001, pp.339–345.
51. Iglesias C, Bodelon OG, Montoya R, et al. Fracture bone healing and biodegradation of AZ31 implant in rats. *Biomed Mater* 2015; 10: 025008.
52. Lamm G, Auer J, Weber T, et al. Postoperative white blood cell count predicts atrial fibrillation after cardiac surgery. *J Cardiothorac Vasc Anesth* 2006; 20: 51–56.
53. Mushahary D, Sravanthi R, Li Y, et al. Zirconium, calcium, and strontium contents in magnesium based biodegradable alloys modulate the efficiency of implant-induced osseointegration. *Int J Nanomed* 2013; 8: 2887–2902.
54. Hou L, Li Z, Pan Y, et al. In vitro and in vivo studies on biodegradable magnesium alloy. *Progr Nat Sci: Mater Int* 2014; 24: 466–471.
55. Zhang E, Xu L, Yu G, et al. In vivo evaluation of biodegradable magnesium alloy bone implant in the first 6 months implantation. *J Biomed Mater Res* 2009; 90: 882–893.
56. Hartwig A. Role of magnesium in genomic stability. *Mutation Res/Fundamental Mol Mech Mutagenesis* 2001; 475: 113–121.
57. Li HF, Xie XH, Zhao K, et al. In vitro and in vivo studies on biodegradable CaMgZnSrYb high-entropy bulk metallic glass. *Acta Biomater* 2013; 9: 8561–8573.
58. Habibovic P and Barralet JE. Bioinorganics and biomaterials: bone repair. *Acta Biomater* 2011; 7: 3013–3026.
59. Hoppe A, Guldal NS and Boccaccini AR. A review of the biological response to ionic dissolution products from bioactive glasses and glass-ceramics. *Biomaterials* 2011; 32: 2757–2774.
60. Rim KT, Koo KH and Park JS. Toxicological evaluations of rare earths and their health impacts to workers: a literature review. *Safety Health Work* 2013; 4: 12–26.
61. Hirano S and Suzuki KT. Exposure, metabolism, and toxicity of rare earths and related compounds. *Environ Health Perspect* 1996; 104: 85–95.
62. Angrisani N, Reifenrath J, Zimmermann F, et al. Biocompatibility and degradation of LAE442-based magnesium alloys after implantation of up to 3.5 years in a rabbit model. *Acta Biomater* 2016; 44: 355–365.
63. Amerstorfer F, Fischerauer SF, Fischer L, et al. Long-term in vivo degradation behavior and near-implant distribution of resorbed elements for magnesium alloys WZ21 and ZX50. *Acta Biomater* 2016; 42: 440–450.
64. Turyanskaya A, Rauwolf M, Grunewald TA, et al. mu XRF elemental mapping of bioresorbable magnesium-based implants in bone. *Materials* 2016; 9: 11.
65. Choudhary L and Singh Raman RK. Magnesium alloys as body implants: fracture mechanism under dynamic and static loadings in a physiological environment. *Acta Biomater* 2012; 8: 916–923.
66. Kannan MB and Raman RKS. In vitro degradation and mechanical integrity of calcium-containing magnesium alloys in modified-simulated body fluid. *Biomaterials* 2008; 29: 2306–2314.
67. Choudhary L, Singh Raman RK, Hofstetter J, et al. In-vitro characterization of stress corrosion cracking of aluminium-free magnesium alloys for temporary bio-implant applications. *Mater Sci Eng C Mater Biol Appl* 2014; 42: 629–636.
68. Levesque J, Hermawan H, Dube D, et al. Design of a pseudo-physiological test bench specific to the development of biodegradable metallic biomaterials. *Acta Biomater* 2008; 4: 284–295.
69. Chen Y, Zhang S, Li J, et al. Dynamic degradation behavior of MgZn alloy in circulating m-SBF. *Mater Lett* 2010; 64: 1996–1999.
70. Hollinger J and Wong ME. The integrated processes of hard tissue regeneration with special emphasis on fracture healing. *Oral Surg, Oral Med, Oral Pathol, Oral Radiol Endodontics* 1996; 82: 594–606.
71. Shaw BA. *Corrosion resistance of magnesium alloys. ASM Handbook – corrosion: fundamentals, testing, and protection*. Materials Park: ASM International, 2003, pp.692–696.
72. Janin R, Nina A, Nina E, et al. Degrading magnesium screws ZEK100: biomechanical testing, degradation analysis and soft-tissue biocompatibility in a rabbit model. *Biomed Mater* 2013; 8: 045012.
73. Witte F, Fischer J, Nellesen J, et al. In vitro and in vivo corrosion measurements of magnesium alloys. *Biomaterials* 2006; 27: 1013–1018.
74. Buckwalter JAET, Bolander ME, Cruess RL, et al. Healing of the musculoskeletal tissues. In: Rockwood CA (ed.) *Rockwood and green's fractures in adults*. Philadelphia: Lippincott-Raven, 1996, pp.261–304.
75. Waizy H, Diekmann J, Weizbauer A, et al. In vivo study of a biodegradable orthopedic screw (MgYREZr-alloy) in a rabbit model for up to 12 months. *J Biomater Appl* 2014; 28: 667–675.
76. Kuhlmann J, Bartsch I, Willbold E, et al. Fast escape of hydrogen from gas cavities around corroding magnesium implants. *Acta Biomater* 2013; 9: 8714–8721.
77. Sfeir C, Ho L, Doll BA, et al. Fracture repair. In: Lieberman JR and Friedlaender GE (eds) *Bone regeneration and repair: biology and clinical applications*. Totowa, NJ: Humana Press, 2005, pp.21–44.
78. Madison M and Martin RB *Fracture healing*. In: Chapman MW and Madison M (eds) *Operative orthopaedics*. Philadelphia: J.B. Lippincott Company, 1993, pp. 221–228.
79. Yoshizawa S, Brown A, Barchowsky A, et al. Magnesium ion stimulation of bone marrow stromal cells enhances osteogenic activity simulating the effect of magnesium alloy degradation. *Acta Biomater* 2014; 10: 2834–2842.
80. Witte F, Ulrich H, Rudert M, et al. Biodegradable magnesium scaffolds: part I: appropriate inflammatory response. *J Biomed Mater Res* 2007; 81: 748–756.
81. Seitz J-M, Lucas A and Kirschner M. Magnesium-based compression screws: a novelty in the clinical use of implants. *JOM* 2016; 68: 1177–1182.